

# Ternary Nanoswitches Realized with Multiresponsive PMMA-*b*-PNIPMAM Films in Mixed Water/Acetone Vapor Atmospheres

Christina Geiger, Julija Reitenbach, Cristiane Henschel, Lucas P. Kreuzer, Tobias Widmann, Peixi Wang, Gaetano Mangiapia, Jean-François Moulin, Christine M. Papadakis, André Laschewsky, and Peter Müller-Buschbaum\*

To systematically add functionality to nanoscale polymer switches, an understanding of their responsive behavior is crucial. Herein, solvent vapor stimuli are applied to thin films of a diblock copolymer consisting of a short poly(methyl methacrylate) (PMMA) block and a long poly(*N*-isopropylmethacrylamide) (PNIPMAM) block for realizing ternary nanoswitches. Three significantly distinct film states are successfully implemented by the combination of amphiphilicity and co-nonsolvency effect. The exposure of the thin films to nitrogen, pure water vapor, and mixed water/acetone (90 vol%/10 vol%) vapor switches the films from a dried to a hydrated (solvated and swollen) and a water/acetone-exchanged (solvated and contracted) equilibrium state. These three states have distinctly different film thicknesses and solvent contents, which act as switch positions “off,” “on,” and “standby.” For understanding the switching process, time-of-flight neutron reflectometry (ToF-NR) and spectral reflectance (SR) studies of the swelling and dehydration process are complemented by information on the local solvation of functional groups probed with Fourier-transform infrared (FTIR) spectroscopy. An accelerated responsive behavior beyond a minimum hydration/solvation level is attributed to the fast build-up and depletion of the hydration shell of PNIPMAM, caused by its hydrophobic moieties promoting a cooperative hydration character.


## 1. Introduction

While switches with complex functions are easily realized in the macroworld, their nanoscale analogs are more challenging to be achieved. Among the possible materials for nanoswitches, thin polymer films mark an interesting class as they offer advantages such as being potentially cheap in production, and the easy integration into existing thin-film technologies.

In particular, stimuli-responsive polymers have gained interest in this context, as they undergo significant changes of their conformation and/or change of their functionality upon a slight change of the external conditions.<sup>[1–3]</sup> When the former changes are used as output signal, the latter ones may serve as the trigger of the nanoswitch. Moreover, different stimuli or a combination of stimuli can lead to different effects for the same stimuli-responsive polymer, resulting in multiresponsive systems.<sup>[4]</sup> This can increase the possibilities for switching polymers such as poly

C. Geiger, J. Reitenbach, L. P. Kreuzer, T. Widmann, P. Wang, Prof. P. Müller-Buschbaum  
Lehrstuhl für Funktionelle Materialien  
Physik-Department  
Technische Universität München  
James-Franck-Str. 1, 85748 Garching, Germany  
E-mail: muellerb@ph.tum.de

C. Henschel, Prof. A. Laschewsky  
Institut für Chemie  
Universität Potsdam  
Karl-Liebknecht-Str. 24-25, 14476 Potsdam-Golm, Germany

 The ORCID identification number(s) for the author(s) of this article can be found under <https://doi.org/10.1002/adem.202100191>.

© 2021 The Authors. Advanced Engineering Materials published by Wiley-VCH GmbH. This is an open access article under the terms of the Creative Commons Attribution-NonCommercial License, which permits use, distribution and reproduction in any medium, provided the original work is properly cited and is not used for commercial purposes.

Dr. G. Mangiapia, Dr. J.-F. Moulin  
German Engineering Materials Science Center (GEMS)  
Helmholtz-Zentrum Hereon outstation at Heinz  
Maier-Leibnitz Zentrum (MLZ)  
Lichtenbergstr. 1, 85748 Garching, Germany

Prof. C. M. Papadakis  
Fachgebiet Physik weicher Materie  
Physik Department  
Technische Universität München  
James-Franck-Str. 1, 85748 Garching, Germany

Prof. A. Laschewsky  
Fraunhofer Institut für Angewandte Polymerforschung IAP  
Geiselbergstr. 69, 14476 Potsdam-Golm, Germany

Prof. P. Müller-Buschbaum  
Heinz Maier-Leibnitz Zentrum (MLZ)  
Technische Universität München  
Lichtenbergstr. 1, 85748 Garching, Germany

DOI: 10.1002/adem.202100191

(*N*-isopropylacrylamide) (PNIPAM) and its structural analog poly(*N*-isopropylmethacrylamide) (PNIPMAM), which are most known for their thermoresponsive properties in aqueous media.<sup>[5–8]</sup> Importantly, they are also sensitive to other stimuli such as changes in pressure,<sup>[9]</sup> salinity<sup>[10]</sup> (according to the Hofmeister series), or composition of the solvent, for instance, the addition of organic cosolvents<sup>[11]</sup> (cosolvency and co-nonsolvency effects).<sup>[12–16]</sup>

As of now, many stimuli-responsive polymers have been successfully synthesized and characterized, and often the polymer configuration has been tailored additionally to fit to the requirements of given applications. To name a few examples, doubly thermoresponsive block copolymers were used as micellar systems for biomedical applications,<sup>[17,18]</sup> grafted nanopatterned brushes were used for controlled biointerfacial interactions (e.g., for bacteria “attach and kill” mechanisms),<sup>[19]</sup> various architectures served as drug delivery systems,<sup>[20]</sup> grafted and spin-coated films were used in surface engineering,<sup>[21–23]</sup> and hydrogels were applied in tissue engineering<sup>[24]</sup> and autonomous sensors.<sup>[25–27]</sup> Microgel films and other specialized systems served as functional cell substrates.<sup>[28–30]</sup> Thin stimuli-responsive polymer films are particularly well suited to form the basis for nanoswitches, as they exhibit faster response times compared to the respective bulk hydrogels and microgels.<sup>[31–34]</sup> Block copolymer thin films in particular offer a good balance between mechanical stability and sensitivity, i.e., the accessible degree of swelling, compared with homopolymer films.<sup>[35,36]</sup>

To establish ternary nanoswitches, meaning thin films which can be brought into three different film thickness states, thin stimuli-responsive polymer films appear very attractive. Binary nanoswitches were realized by the swelling and collapse of thin thermoresponsive polymer films, which enabled two controlled film thickness values representing “on” and “off” states of the nanoswitch.<sup>[35,36]</sup> Adding to this a co-nonsolvency approach, three different film thicknesses can be established via a dried, a fully hydrated, and a water/cosolvent-exchanged state. These distinct three states can be used, for example, as nanoswitch positions, “off” (dried state), “on” (hydrated state), and “standby” (water/cosolvent-exchanged state), thereby constituting a ternary nanoswitch. Other scenarios requiring three switching positions, such as configuring between three channels, are also possible.

To demonstrate this concept, we use thin films of a responsive diblock copolymer, which consists of a short water-insoluble poly(methyl methacrylate) (PMMA) and a long water-soluble poly(*N*-isopropylmethacrylamide) (PNIPMAM) block. The PMMA block is kept short to enhance the mechanical stability of the thin films without compromising responsive behavior. The amphiphilic polymer PNIPMAM is selected as the longer block, as it is able to take up and release water easily, due to hydrophobic hydration effects around the methyl moiety in the polymer backbone and the isopropyl moiety in the side chain lowering the energetic barrier separating the attachment and detachment of water molecules. The three different thin-film equilibrium states are investigated by static time-of-flight neutron reflectometry (ToF-NR) measurements, whereas the kinetics of vapor-induced swelling and switching are determined with kinetic ToF-NR and spectral reflectance (SR) measurements. Additional information about the solvation processes at the PNIPMAM amide and isopropyl functional groups is gained from Fourier-transform infrared (FTIR) spectroscopy.

## 2. Concept of Ternary Polymer Nanoswitches

The aim of the present study is to probe the swelling behavior and switching kinetics of thin films of a stimuli-responsive PNIPMAM-based diblock copolymer and assess the suitability of such films to be used in nanoswitches with extended functionality. To induce film swelling and contraction, the polymer layer is exposed to water vapor and mixed water/cosolvent vapors. To function as the active (actuating) layer of a switch, i.e., to move the switch into the available positions with good control, the resulting equilibrium degrees of swelling of the thin film have to be well defined (sufficiently different from each other). Also, ideally, these positions should be reached on a fast time-scale. Compared to binary switches, with “on” and “off” positions, ternary devices feature a third available position and are used, e.g., for configuring between channels “one,” “two,” and “three” or automatic switching between “on,” “standby,” and “emergency off” positions. To realize this additional functionality of three positions, the amphiphilicity as well as the co-nonsolvency effect of the PNIPMAM block are utilized, so that each switching position corresponds to a distinct state of the polymer thin film, respectively: the dried state, the water-hydrated (solvated and swollen) state, and the water/cosolvent-exchanged (solvated but contracted) state.

The diblock copolymer poly(methyl methacrylate)-*block*-poly(*N*-isopropylmethacrylamide) (PMMA-*b*-PNIPMAM), featuring a short PMMA block and a long PNIPMAM block, is selected as stimuli-responsive material. Its chemical structure is shown in **Figure 1**. The synthesis and molecular analysis of PMMA-*b*-PNIPMAM are provided in detail in the Supporting Information.

The permanently hydrophobic PMMA block not only adds mechanical stability to the films, which is essential for the application in switches and other devices, but also facilitates the preparation of smooth films by spin coating from solution (see Experimental Section for details about the sample preparation), compared with films made from the PNIPMAM homopolymer (often, a combination of spin coating and solvent vapor annealing is required to achieve homogeneous films, as shown in the study by Kreuzer et al.<sup>[37]</sup>).

The PNIPMAM block provides the stimuli-responsive part of the block copolymer. Both hydrophobic moieties (methyl residue on the polymer backbone and isopropyl residue in the side chain) and hydrophilic moieties (amide group in the side chain) are present in the constitutional repeating unit. The resulting delicate balance between intra- and intermolecular polymer-polymer interactions as well as repulsive and attractive interactions with water or water/cosolvent mixtures leads to the amphiphilic properties<sup>[6,38,39]</sup> and the co-nonsolvency behavior<sup>[37,40]</sup> of PNIPMAM. These two aspects are described in more detail in the following paragraphs.

The amphiphilic properties and thermoresponsive behavior of the PNIPMAM homopolymer were previously characterized in aqueous solution,<sup>[6,38,39,41–45]</sup> as well as in thin-film configuration,<sup>[37,46]</sup> and were investigated via molecular dynamics simulations and quantum mechanical calculations.<sup>[44,47]</sup> The energy barriers for attaching and detaching water molecules, which form hydrogen bonds with the amide group and are structured in cages around the hydrophobic moieties (an effect known as hydrophobic hydration<sup>[42,48]</sup>), are low. Therefore, the hydration

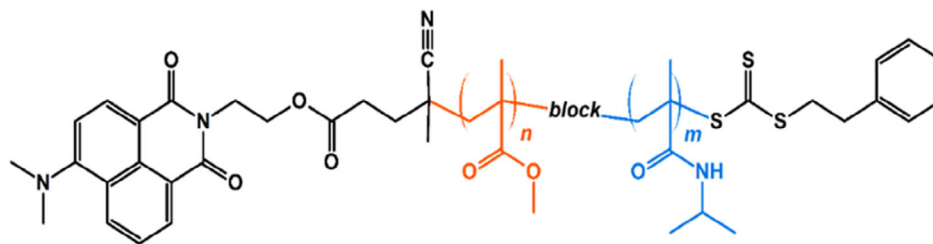


**Figure 1.** Chemical structure of the used diblock copolymer  $\text{PMMA}_n\text{-}b\text{-PNIPAM}_m$ , including the RAFT chain transfer agent's R-group and Z-group. The number average degrees of polymerization  $DP_n$ , as determined by UV-vis, are  $n = 23$  for the PMMA block (red) and  $m = 323$  for the PNIPAM block (blue).

shell around PNIPAM can be easily built up and depleted. This is accompanied by a significant conformational change of the polymer chain and a large change in the occupied volume. In aqueous solution, due to the aforementioned mechanism, PNIPAM undergoes a reversible coil-to-globule phase transition upon heating past the lower critical solution temperature (LCST), that is followed by a further aggregation into mesoglobules.<sup>[45]</sup> Compared with its more popular polymer analog PNIPAM,<sup>[7,8]</sup> the LCST of PNIPAM in aqueous solutions is shifted to higher temperatures ( $\text{LCST}_{\text{PNIPAM}} \approx 32^\circ\text{C}$ ,  $\text{LCST}_{\text{PNIPAM}} \approx 44^\circ\text{C}$ ), and the cloud points ( $T_{\text{CP}}$ ) of PNIPAM solutions are less dependent on molar mass, polymer concentration, or added electrolytes.<sup>[7]</sup> In the one-phase state (below  $T_{\text{CP}}$ ), PNIPAM chains are more hydrated and expanded, compared with PNIPAM, whereas in the two-phase state (above  $T_{\text{CP}}$ ), PNIPAM forms larger and more loosely packed mesoglobules.<sup>[45]</sup> In addition, the intra- and intermolecular interactions between PNIPAM amide groups were found to be weaker.<sup>[44,47]</sup> In thin PNIPAM films, the transition temperature (TT, onset of film contraction) was found at lower values (TT  $\approx 38^\circ\text{C}$ , PNIPAM thin films in  $\text{D}_2\text{O}$  vapor<sup>[46]</sup>) than in solutions, in agreement with the trend established for increasing polymer concentration. Large amounts of water were taken up, when going from the dried (e.g., dried under a nitrogen flow) to the hydrated film state (in saturated water vapor), or released, when changing from the hydrated to the dehydrated film state by heating above the TT. Due to the fixed surface area, a significant change in film thickness was observed both during the film hydration and dehydration processes.<sup>[46]</sup>

Upon the addition of different organic cosolvents, the LCST or TT of poly(acrylamides) was reported to shift in dependence on the molar fraction of the cosolvent.<sup>[11]</sup> Moreover, a co-nonsolvency effect was found, i.e., a decrease in solubility of the polymer in the solvent mixture within a certain compositional range, which causes a coil-to-globule transition or even precipitation in solution or a contraction in thin films (both for PNIPAM<sup>[11,15,16,21,22,49]</sup> and PNIPAM<sup>[37,40]</sup> solutions and thin films). Up to now, the molecular mechanisms of the co-nonsolvency phenomenon have not yet been fully clarified, and various explanations are subject of current scientific debate.<sup>[50–54]</sup> However, the co-nonsolvency effect was exploited across many disciplines of science. For example, it was used in surface engineering and for the capture and release of nanoparticles,<sup>[21,22]</sup> for the selective precipitation of DNA,<sup>[55]</sup> for tunable polymer matrices,<sup>[56]</sup> for the detection of volatile organic solvents,<sup>[57]</sup> and for other applications.<sup>[58,59]</sup>

For investigations with simultaneous ToF-NR/SR measurements, thin films of  $\text{PMMA}_n\text{-}b\text{-PNIPAM}_m$  (film thickness  $d = (140 \pm 5)$  nm, in dried equilibrium) are deposited onto silicon substrates via the spin-coating method. Samples used for FTIR spectroscopy measurements are prepared by drop casting (for further information, see Experimental Section).

To change the thin films from a dried to a hydrated and water/cosolvent-exchanged state, the films are exposed to a gas flow with constant flow rate and adjustable composition, mixed from  $\text{N}_2$ , saturated water vapor and cosolvent (acetone) vapor streams. This allows examination of the swelling process induced by hydration and the contraction process induced by the co-nonsolvency effect. The solvent gas flow protocol, as shown in **Figure 2**, is applied for both in situ ToF-NR/SR measurements, as well as for FTIR spectroscopy experiments.

After drying in 100 vol%  $\text{N}_2$  for 1 h, the dried equilibrium stage (I) is reached and measured. Next, the hydration process (II) in 100 vol% water vapor is initiated and measured for 350 min, until the films adopted the hydrated equilibrium state (III). Then, the solvent vapor composition is changed to water/acetone (90 vol%/10 vol%), and the exchange process (IV) is probed for 150 min, until the films arrived in the final water/acetone-exchanged equilibrium stage (V). All experiments are conducted at a constant temperature of  $18^\circ\text{C}$ .

Heavy water ( $\text{D}_2\text{O}$ ) is used for hydration (by virtue of a large scattering contrast in ToF-NR). Acetone and acetone- $\text{d}_6$  are applied as organic co-solvents for ToF-NR/SR measurements (scattering contrast between  $\text{D}_2\text{O}$  and acetone) and FTIR spectroscopy (to avoid signal overlap with the C–H<sub>3</sub> asymmetric isopropyl stretching vibration signal of the polymer),

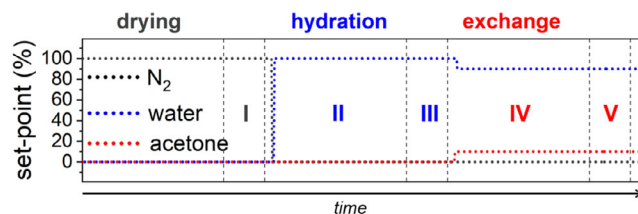


**Figure 2.** Schematic gas flow protocol used in simultaneous ToF-NR/SR and FTIR measurements. Roman numerals are equivalent to different stages of the thin-film response: dried equilibrium (I) using 100 vol%  $\text{N}_2$ , hydration process and hydrated equilibrium (II + III) using 100 vol% water vapor, and water/acetone-exchange process and water/acetone-exchanged equilibrium (IV + V) using water/acetone (90 vol%/10 vol%) vapor.

respectively. Acetone is selected, as it has a high vapor pressure, allowing easy vapor generation, is fully miscible with water, and readily available in its deuterated form due to its usage as NMR solvent. As it is an aprotic solvent, an H/D exchange between the water and cosolvent species is very slow and can be excluded, which allowed circumnavigating a mixture-dependent scattering length density (SLD) of the individual solvents. Supplementary SR measurements using solvent vapors with alternate isotopic compositions are carried out to evaluate the impact of isotopic effects<sup>[60,61]</sup> on the film swelling behavior (see Section 3.2.2. and Figure S4, Supporting Information).

### 3. Results and Discussion

#### 3.1. Thin-Film Equilibrium States

The dried (I), D<sub>2</sub>O-hydrated (III), and D<sub>2</sub>O/acetone-exchanged (V) equilibrium film states are probed with static ToF-NR measurements. The obtained specular reflectivity  $R(q_z)$  is analyzed with a multilayer model (six layers, also see in the SI), yielding the SLD profile of the film along the surface normal  $z$ . The film thickness  $d$ , water and acetone content in the bulk  $\Phi_{\text{solvent}}$ , solvent fraction within the solvent content  $x$ , as well as solvent gradients toward the polymer–substrate and polymer–air interfaces are determined. Further information on the ToF-NR measurements, instrumentation, and data analysis is presented in the Experimental Section as well as in the Supporting Information. In **Figure 3**, the full reflectivity data (Figure 3a), details of the reflectivity at low  $q_z$  values (for a better display of the  $q_z$  position of the critical edge of total reflection and spacing and amplitude of Kiessig fringes, Figure 3b), and SLD profiles (Figure 3c) obtained for the three film equilibrium states (at 18 °C) are shown.

Due to the high SLD of D<sub>2</sub>O ( $\text{SLD}_{\text{D}_2\text{O}} = 6.335 \times 10^{-6} \text{ \AA}^{-2}$ ), the critical edge shifts to a higher  $q_z$  value as the films move from the dried (I) to the D<sub>2</sub>O-hydrated (III) state, and the spacing of Kiessig fringes becomes smaller. This indicates the incorporation of substantial amounts of water into the film, accompanied by a significant increase in film thickness. A reverse effect,

**Table 1.** Film thickness  $d$  and bulk layer SLD during the equilibrium states, as determined from fits of the static ToF-NR data shown in Figure 3.

Film state	$d$ [nm]	Bulk layer SLD [ $10^{-6} \text{ \AA}^{-2}$ ]
Dried (I)	$140.7 \pm 0.3$	$0.66 \pm 0.03$
D <sub>2</sub> O hydrated (III)	$264.1 \pm 0.9$	$3.51 \pm 0.01$
D <sub>2</sub> O/acetone exchanged (V)	$187.2 \pm 2.4$	$2.25 \pm 0.01$

both regarding the position of the critical edge and the spacing of Kiessig fringes, is observed as the films adopt the D<sub>2</sub>O/acetone-exchanged equilibrium (V), signifying a release of solvent and film contraction.

The SLD profiles, corresponding to the fits of the measured reflectivity data, contain detailed information on the vertical distribution of solvents and polymer. The fit results for the film thickness  $d$  and bulk layer SLD are shown in **Table 1**. Three distinctly different thin film equilibrium states are observed, which correspond to the aspired three states (“on,” “off,” and “standby”) of a nanoswitch. The diblock copolymer film underwent a swelling process (dry-to-swollen state) in D<sub>2</sub>O vapor, but a contraction (swollen-to-exchanged state) in mixed D<sub>2</sub>O/acetone vapor, whereby the swelling ratio and the solvent content differ markedly for the D<sub>2</sub>O-hydrated and D<sub>2</sub>O/acetone-exchanged states. **Table 2** shows the film swelling ratio  $d/d_{\text{ini}}$ , with the initial film thickness  $d_{\text{ini}} = 140.7 \text{ nm}$  (dried equilibrium state’s film thickness), the solvent content in the bulk  $\Phi_{\text{solvent}}$ , and the acetone fraction within the solvent content  $x$ .

The SLD profile of the dried polymer film shows that the film has a homogeneous polymer density along the surface normal, with a minor decrease toward the polymer–substrate interface. The calculated theoretical neutron SLD value of the diblock polymer is  $0.813 \times 10^{-6} \text{ \AA}^{-2}$ , assuming a polymer density of  $1.0 \text{ g cm}^{-3}$ . Thus, it is larger than the measured SLD value of  $0.66 \times 10^{-6} \text{ \AA}^{-2}$  of the film in the dried equilibrium state. We attribute this difference to the presence of residual H<sub>2</sub>O ( $\text{SLD}_{\text{H}_2\text{O}} = -0.561 \times 10^{-6} \text{ \AA}^{-2}$ ), which the film took up in ambient conditions and which is not removable by drying the film in a

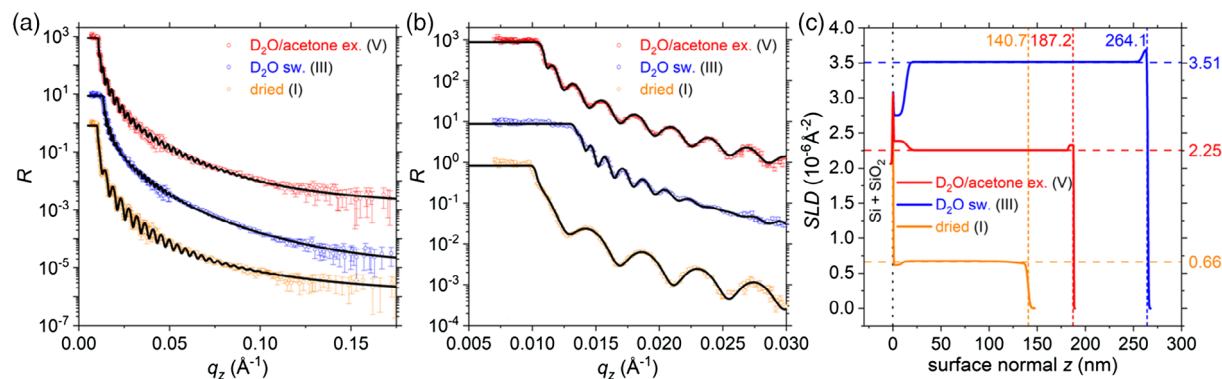


**Figure 3.** Results of static ToF-NR measurements of PMMA-*b*-PNIPAM thin films: a) Full reflectivity data  $R(q_z)$  and b) details at low  $q_z$  illustrating the shift of the critical edge of total reflection and changes within the spacing of Kiessig fringes, measured in dried (orange), D<sub>2</sub>O-hydrated (blue), and D<sub>2</sub>O/acetone-exchanged equilibrium (red) at 18 °C (I, III, and V, respectively; refer to the stages from the gas flow protocol). The curves are vertically shifted for clarity. Fits of the data are presented as solid black lines. c) Corresponding SLD profiles with dashed lines which indicate the total film thickness  $d$  and SLD values of the main polymer layer.

**Table 2.** Film swelling ratio  $d/d_{ini}$ , solvent content  $\Phi_{solvent}$ , and acetone fraction within the solvent content  $x$  during the equilibrium states, as calculated from ToF-NR results.

Film state	Film swelling ratio $d/d_{ini}$	Solvent content $\Phi_{solvent}$	Acetone fraction within solvent content $x$ [vol%]
Dried (I)	1.00	n.a.	n.a.
D <sub>2</sub> O hydrated (III)	1.87	0.47	0.00
D <sub>2</sub> O/acetone exchanged (V)	1.33	0.25	6.56

N<sub>2</sub> flow even after 1 h of drying at the temperature of the experiments of 18 °C. The steric hindrance of the additional methyl group on the PNIPMAM backbone, causing an increased rigidity of the polymer chains, compared with PNIPAM, may contribute to the residual H<sub>2</sub>O in the copolymer film.

The obtained SLD profile of the diblock copolymer film in the D<sub>2</sub>O-hydrated state supports this explanation: Usually, solvent enrichment layers are observed toward the interfaces in the hydrated equilibrium state of responsive thin films.<sup>[60–62]</sup> In the present study, a D<sub>2</sub>O enrichment is found at the polymer–air interface, indicated by an increased SLD, as was expected.<sup>[60–62]</sup> However, at the polymer–silicon substrate interface, the opposite occurs with the SLD value being lower than that of the average D<sub>2</sub>O-containing polymer film. Its exact value arises from the presence of H<sub>2</sub>O, which accumulated in proximity to the native hydrophilic SiO<sub>2</sub> layer of the substrate, and is exchanged at a slower rate compared with the water species in proximity of the constant D<sub>2</sub>O vapor flow.

In the exchanged equilibrium state, a homogeneous SLD is found for the polymer layer, indicating an equilibration of the D<sub>2</sub>O/acetone mixture along the film normal. For the D<sub>2</sub>O/acetone-exchanged equilibrium film state, enrichment layers of a solvent mixture with a high D<sub>2</sub>O fraction are observed toward both interfaces. Thus, three distinct film states are successfully prepared by the combination of the amphiphilicity

and the co-nonsolvency effect of the PNIPMAM block on the PMMA-*b*-PNIPMAM thin films.

### 3.2. Vapor-Induced Swelling and Switching Characteristics

In addition to the existence of three states for the nanoswitches realized by the PMMA-*b*-PNIPMAM thin films, also the kinetics of reaching these film states is a crucial aspect. Using simultaneous kinetic ToF-NR and SR measurements, changes of the thin films are probed during the D<sub>2</sub>O hydration (II) and D<sub>2</sub>O/acetone-exchange processes (IV). A time resolution of 10 s is chosen for SR measurements, and kinetic ToF-NR data are binned to 30 s. In general, the results obtained in situ via static and kinetic ToF-NR and SR are in good agreement. Note that slight deviations are to be expected between ToF-NR and SR, due to the differences within the recorded data (using visible light vs neutrons as a probe and different sampled area) and the weighting of data points in the respective fitting algorithms.

In **Figure 4**, the evolution of the film thickness  $d$  (Figure 4a) and (optical) refractive index  $n$  (Figure 4b), as determined by SR, are shown. In addition, in Figure 4a, the film thicknesses of the film equilibrium states, obtained with static ToF-NR, are marked with dashed horizontal lines, and intermediate film states, corresponding to selected kinetic ToF-NR data (see **Figure 5**), are indicated with letters (from A to K) for the swelling and (from L to P) for the contraction processes.

The SLD profiles obtained from the respective ToF-NR curves are shown in **Figure 6** for the film swelling (Figure 6a) and the film contraction (Figure 6b).

The observed film swelling process in D<sub>2</sub>O vapor can be divided into two phases due to the different kinetics. Initially, the film swelling is slow (first phase, from A to C), followed by a rapid swelling (second phase, from D to K), until the maximum film thickness (hydrated equilibrium state) is reached. While the film swelling suggests to be a two-step process, the film contraction occurs as a single step and is a very rapid process. The changes in film thickness match well with the changes found in the refractive index of the polymer layer.

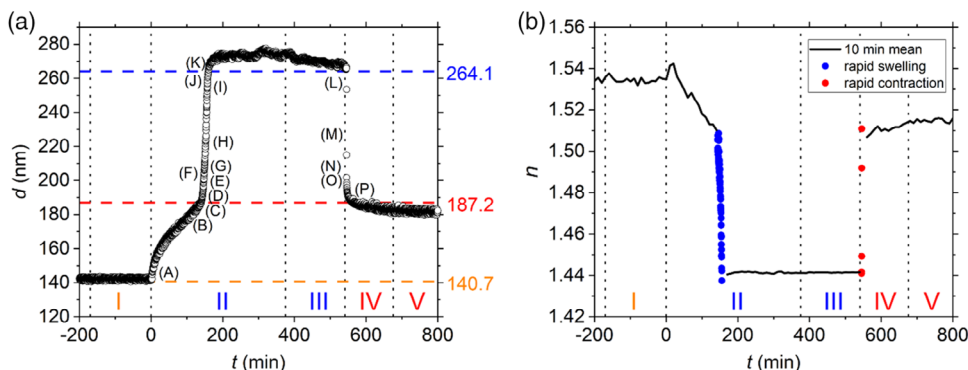


**Figure 4.** Temporal evolution of a) the film thickness  $d$  and b) the refractive index  $n(\lambda = 500 \text{ nm})$ , as determined by in situ SR of the thin PMMA-*b*-PNIPMAM film during dried equilibrium (I), D<sub>2</sub>O hydration process and hydrated equilibrium (II + III), and D<sub>2</sub>O/acetone-exchange process and -exchanged equilibrium (IV + V). Horizontal dashed lines in (a) indicate the film thickness  $d$ , as determined by static ToF-NR measurements during dried (orange), D<sub>2</sub>O-hydrated (blue), and D<sub>2</sub>O/acetone-exchanged equilibrium (red) (I, III, and V, respectively). Vertical dashed lines are intended as a guide to the timeline of the experiment (initiation of the hydration stage is taken as time zero). Intermediate states (see **Figure 5**) are indicated with letters (from A to K) for the swelling and (from L to P) for the contraction processes. In (b), data obtained during the phases of rapid film swelling and contraction are displayed for each measurement point; the other data are averaged (10 min) for readability of the graph.

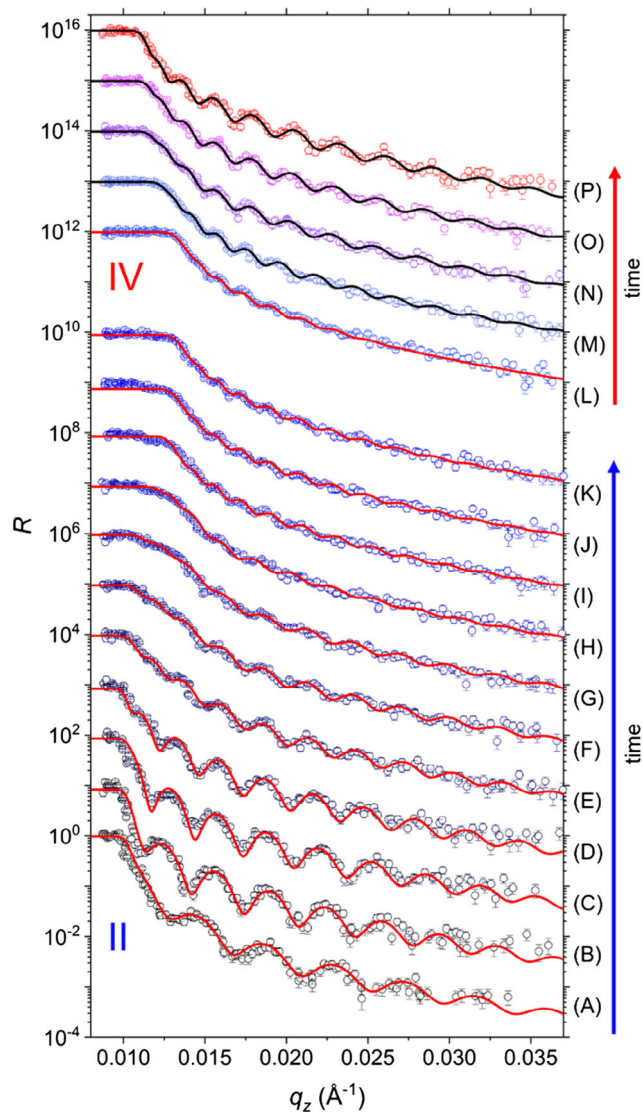


**Figure 5.** Selected kinetic ToF-NR curves acquired during the D<sub>2</sub>O hydration (II) and D<sub>2</sub>O/acetone-exchange processes (IV). The curves are vertically shifted for clarity (bottom to top/color gradient: black [dried] to blue [hydrated] to red [exchanged]). Fits to the data are shown as solid lines. Letters (A to K, during water swelling, and L to P, during solvent exchange) mark the selected intermediate film states (also see Figure 4a and Table 3).

We noted a slight increase of the refractive index at the start of the swelling process, which may be due to the accumulation of water at the polymer–air interface, which was previously removed by drying (i.e., the temporary increase is attributed to the polymer–air interfacial roughness becoming a polymer–water interfacial gradient).

As is expected for the incorporation of D<sub>2</sub>O ( $n_{D_2O} = 1.33$ ), the overall refractive index of the polymer layer decreases ( $n_{ini} = 1.53$  [dried equilibrium] and  $n_{meas} = 1.44$  [hydrated equilibrium]). In agreement with the development in film thickness, two phases (first slow, then rapid decrease) are observed. The refractive index change observed during film contraction and the measured value during the D<sub>2</sub>O/acetone-exchanged equilibrium film state ( $n_{meas} = 1.51$ )

are in agreement with the refractive index observed at the onset of the phase of rapid film swelling, indicating that the films exhibit a similar solvation level at these swelling conditions.

Selected kinetic ToF-NR data corresponding to intermediate film states (see Figure 4a and Table 3 for exact timestamps) during the swelling and contraction processes, along with the respective fits to the reflectivity  $R(q_z)$  for each curve, are shown in Figure 5. The continuous shifts in the  $q_z$  position of the critical edge, and the changes in the spacing and amplitude of Kiessig fringes, are in good agreement with expectations for a swelling process induced by D<sub>2</sub>O vapor (II), on the one hand, and film contraction caused by the exchange to a D<sub>2</sub>O/acetone vapor mixture (IV) on the other hand (also see Section 3.1).

During the swelling process, a gradient in the SLD profile develops with an increased SLD value toward the polymer–air interface. This D<sub>2</sub>O gradient is especially pronounced when the slow, first phase of swelling changes to the rapid second phase of swelling. During the latter, the SLD of the bulk polymer layer rapidly increases, and aligns with the SLD of the gradient layer, which reaches the maximum value ahead of the bulk. We attribute the formation of this gradient to a faster exchange of water species at the polymer–air interface, as well as the formation of a D<sub>2</sub>O enrichment layer at this interface.

The onset of the second, rapid film swelling process is interpreted as the point during the swelling kinetics at which, due to a sufficiently large water uptake, the PNIPMAM intra- and intermolecular hydrophobic interactions are mitigated by the presence of water at the hydrophobic moieties to such an extent that a cooperative hydration process can start<sup>[63,64]</sup> (note that due to the presence of the PMMA block, the hydrophobic interactions inside the polymer layer are additionally reinforced). The cooperative hydration in turn results in the acceleration of the swelling rate, and the rapid equilibration of water species within the film, until the maximum amount of water is taken up.

During the film contraction process, again, an SLD gradient is seen at the polymer–air interface, which can be explained. Due to the rapid contraction of the polymer layer induced by the D<sub>2</sub>O/acetone mixture, the solvents are released and exit the film via the polymer–air interface. Due to the co-nonsolvency effect actively driving the film contraction, the shrinking of the polymer layer is faster than the equilibration with the surrounding vapor. This leads to a temporary solvent accumulation at the interface (see intermediate film states M, N, and O). The vertical film composition can be separated into three individual layers (polymer–substrate interfacial layer, bulk layer, and polymer–air interfacial layer) of the film during the rapid swelling and rapid contraction phases. The respective values are shown in Figure S5, Supporting Information.

The acceleration of the swelling rate seen past a minimum swelling ratio, in accordance with the changes in refractive index, and the observed gradient formation, imply that a minimum hydration/solvation level is needed, to enable the operation of nanoswitches inside a swelling regime, which is dominated by cooperative hydration.

To evaluate the possible influence of isotopic effects, supplementary measurements are carried out, in which the hydration and exchange processes are probed with solvent vapors of alternate isotopic composition. The evolution of the film thickness  $d$ , as determined by SR, for the full experimental sequence (I to

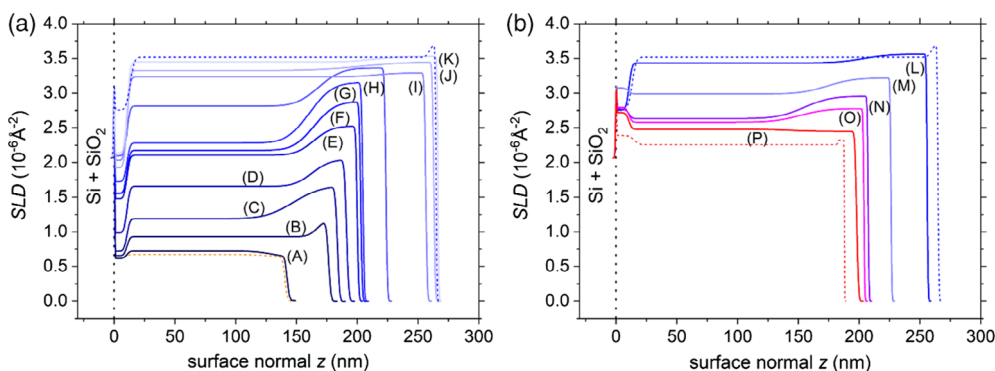


**Figure 6.** Representative SLD profiles of the PMMA-*b*-PNIPMAM thin film, extracted from selected kinetic ToF-NR data (solid lines). a) Profiles during the D<sub>2</sub>O hydration (II); letters A to K indicate successive phases of swelling (color gradient black [dried] to blue [hydrated]). b) Profiles during the D<sub>2</sub>O/acetone exchange processes (IV); letters L to P indicate successive phases of solvent exchange (color gradient blue [hydrated] to red [exchanged]). See also Figure 4a and Table 3. For comparison, SLD profiles of the static ToF-NR data are added as dashed lines for the dried (orange), the hydrated (blue), and the exchanged equilibrium states (red).

**Table 3.** Timestamps of selected intermediate film states probed by simultaneous ToF-NR/SR. Initiation of the hydration stage (II) is taken as time zero.

Letter <sup>a)</sup>	<i>t</i> [min]	Letter <sup>b)</sup>	<i>t</i> [min]
A	0.0	L	545.5
B	106.0	M	546.0
C	123.0	N	546.5
D	143.0	O	548.0
E	146.0	P	600.0
F	147.0		
G	148.0		
H	154.0		
I	156.0		
J	160.0		
K	180.0		

<sup>a)</sup>Hydration (II); <sup>b)</sup>Exchange (IV).

V) using D<sub>2</sub>O and acetone-d<sub>6</sub> vapor, and for the swelling (I and II) in H<sub>2</sub>O vapor, is shown in Figure S4, Supporting Information. These solvent species are selected, as the solvent combination of D<sub>2</sub>O and acetone-d<sub>6</sub> avoids signal overlap in the FTIR spectroscopy measurements. Furthermore, the swelling behavior of thin responsive films in water vapor is known to show an isotopic effect.<sup>[60,61]</sup> In both supplementary measurements, the two-step swelling pattern during the hydration process is found. Also, similar maximum film thicknesses *d* in the hydrated equilibrium are reached, as in the ToF-NR/SR measurement. Notably, while the behavior qualitatively is the same, the onset of the phase of accelerated swelling shifts in time for different samples (in D<sub>2</sub>O vapor after ≈150 min [ToF-NR/SR] and ≈250 min (supplementary SR) and in H<sub>2</sub>O vapor after ≈125 min [supplementary SR]). While this finding exemplifies that the onset of accelerated swelling is very sensitive to the detailed experimental conditions, the observed trend (fastest

onset in H<sub>2</sub>O vapor) generally fits into the expectation of a possible isotopic effect, due to the increased bond strength of hydrogen bonds in H<sub>2</sub>O over D<sub>2</sub>O. The kinetics of the contraction process observed in mixed D<sub>2</sub>O/acetone-d<sub>6</sub> vapor, and the film thickness in the D<sub>2</sub>O/acetone-d<sub>6</sub>-exchanged equilibrium, are comparable with the results with mixed D<sub>2</sub>O/acetone vapor.

### 3.3. Solvation Processes at the PNIPMAM Functional Groups

For a deeper understanding, the development of molecular interactions at the responsive PNIPMAM block as solvent molecules are incorporated and released from the PMMA-*b*-PNIPMAM thin films, is studied in situ with FTIR spectroscopy. Note that the results of simultaneous ToF-NR/SR measurements and FTIR spectroscopy measurements are not fully comparable due to differences in the required film thickness of the samples and the volume of the used sample environment. To obtain a good signal-to-noise ratio, thicker diblock copolymer films are necessary in the FTIR measurements. Also, a sample chamber with a smaller volume is used, leading to a faster equilibration of the vapor composition around the sample (see Experimental Section for the individual sample preparation methods and sample environments). Therefore, we restrict the analysis to the changing local chemical environments at the functional groups.

The recorded FTIR spectra ( $\Delta t = 125$  s) for the hydration of PMMA-*b*-PNIPMAM films induced by D<sub>2</sub>O vapor (II + III) are shown in Figure 7a. The subsequently recorded FTIR spectra during the water/acetone-exchange process within the films, induced by switching to mixed D<sub>2</sub>O/acetone-d<sub>6</sub> vapor (IV + V), are shown in Figure 7b. The emergence and decay of the most intense solvent-specific signal peaks/absorbance bands are indicated with arrows (corresponding water species in blue, acetone-d<sub>6</sub> in red).

To investigate the overall film hydration state and the related changing local chemical environment around the PNIPMAM block, the evolution in the absorbance peak area of the O–D stretching vibration (D<sub>2</sub>O integral) and the peak position shift of selected signals are analyzed. Namely, the secondary amide and isopropyl functional groups within the NIPMAM structural

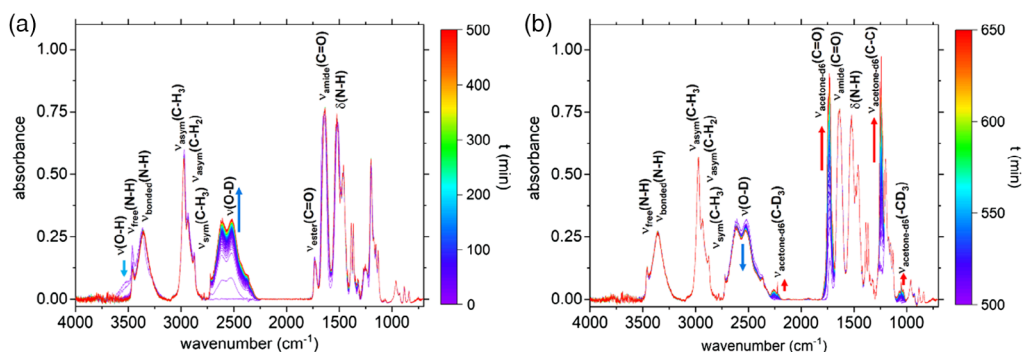


**Figure 7.** FTIR spectra of PMMA-*b*-PNIPMAM films taken during a) hydration using D<sub>2</sub>O vapor and b) solvent exchange using mixed D<sub>2</sub>O/acetone-d<sub>6</sub> vapor. Spectra (color gradient (a) purple [dried] to red [hydrated] and (b) purple [hydrated] to exchanged [red]) are recorded, until the hydrated and exchanged equilibrium states are reached (after 500 min and 650 min, respectively, initiation of the hydration stage (II) is taken as time zero). Arrows indicate the emergence and decay of solvent-specific signals, due to solvent incorporation and release (blue for water species; red for acetone-d<sub>6</sub>).

motif were focused on. To examine the hydration and co-solvent-induced dehydration processes at the amide group, which are dominated by the formation and breakage of hydrogen bonds, two characteristic signals are chosen: the amide I band ( $\nu_{\text{amide}}(\text{C}=\text{O})$ ), located in the wavenumber range  $\nu = 1630\text{--}1650\text{ cm}^{-1}$  and the amide II band ( $\delta(\text{N-H})$ ) in the wavenumber range  $\nu = 1510\text{--}1525\text{ cm}^{-1}$ . To study the process of hydrophobic hydration around the isopropyl group, the asymmetric C-H<sub>3</sub> stretching vibration ( $\nu_{\text{asym}}(\text{C-H}_3)$ ), found

within the wavenumber range  $\nu = 2970\text{--}2975\text{ cm}^{-1}$ , is selected. The change in absorbance peak area of the O-D stretching vibration, and the peak position shifts of the three aforementioned signals, are shown in **Figure 8**, for the full experimental sequence (I–V).

When the film is exposed to pure D<sub>2</sub>O vapor, and then the mixed D<sub>2</sub>O/acetone-d<sub>6</sub> vapor, the peak area of the O-D stretching vibration increases as the film changes from the dried equilibrium state (I) to the hydrated state (II + III). In

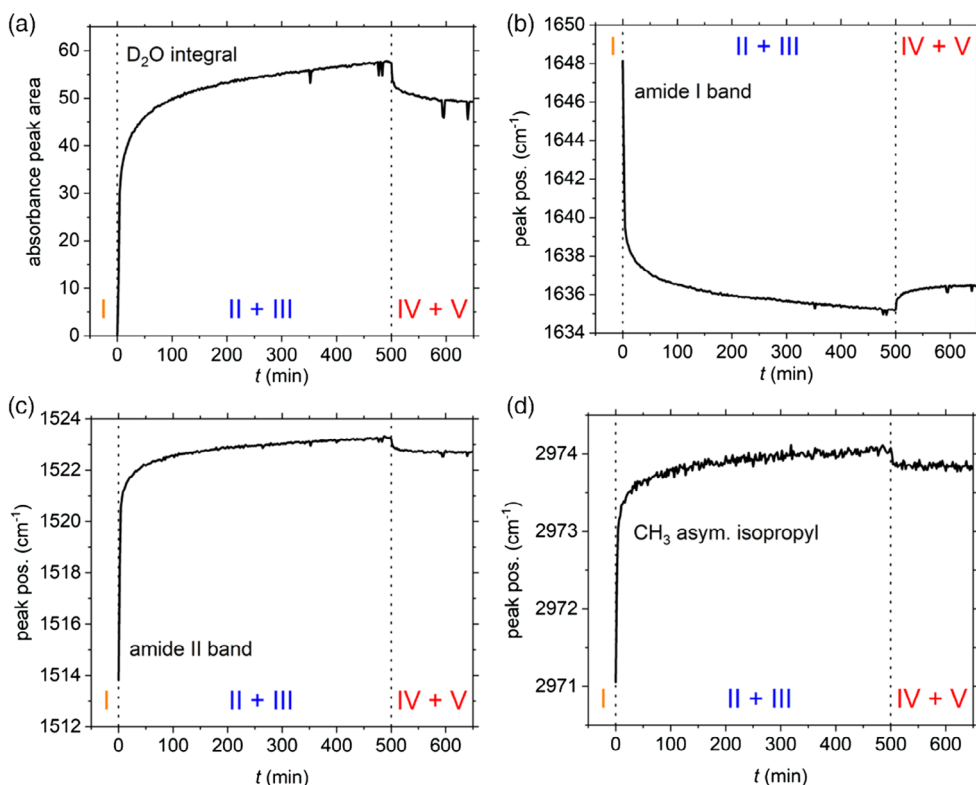


**Figure 8.** Evolution of the FTIR absorbance a) peak area of the O–D stretching vibration signal (labeled D<sub>2</sub>O integral), b) position of the amide I band, c) position of the amide II band, and d) position of the C–H<sub>3</sub> asymmetric isopropyl stretching vibration signal for the dried films (I), hydration with D<sub>2</sub>O vapor (II + III), and exchange to mixed D<sub>2</sub>O/acetone-d<sub>6</sub> vapor (IV + V).



contrast, it decreases as the cosolvent is added and the D<sub>2</sub>O/acetone-d<sub>6</sub>-exchanged state is reached (IV + V). Notably, in the development of the peak area of the O–D stretching vibration, no two-step behavior, as seen in the thickness increase for thin films investigated by simultaneous ToF-NR/SR and SR (see Figure 4 and Figure S4, Supporting Information), is observed. We attribute this difference primarily to the larger film thickness required for FTIR, as discussed earlier. Other influences may also be due to the different timescales of the kinetics of the mesoscopic film swelling and contraction processes compared with the hydration and dehydration processes in the local chemical environment of the PNIPMAM functional groups.

In accordance with the observed incorporation and release of D<sub>2</sub>O, the peak position of the amide I band first shifts toward lower wavenumbers (II + III). Then, this shift is partially reversed (IV + V). For the amide II band and the asymmetric isopropyl stretching vibration, the opposite trends are observed, whereas the wavenumber shift is smallest for the C–H<sub>3</sub> asymmetric isopropyl stretching vibration due to the decreased strength of interaction with D<sub>2</sub>O.

The backshift in the peak position occurs more rapidly for the amide II band and C–H<sub>3</sub> asymmetric isopropyl stretching vibration signal than the amide I band. The concerted, rapid shift of the peak position of the amide II band and C–H<sub>3</sub> asymmetric isopropyl stretching vibration signal supports the hypothesis that the hydration around hydrophobic moieties is a cooperative process and complements the rapid film contraction process seen in ToF-NR/SR measurements. The partial backshift of the amide I band is most slowly, suggesting that the exchange of the C=O-bound water occurs slowest. This is in accordance with previous work on solutions, suggesting that most of the C=O-bound water is able to remain in the two-phase (globule) state, as was reported in the study by Maeda et al.<sup>[42]</sup>

The developments seen for the local chemical environment around the PNIPMAM amide and isopropyl functional groups are in good agreement with the expectations for film swelling induced by hydration in D<sub>2</sub>O vapor and a co-nonsolvency-related rapid contraction and exchange induced by mixed D<sub>2</sub>O/acetone-d<sub>6</sub> vapor.

## 4. Conclusion

Ternary nanoswitches are realized using PMMA-*b*-PNIPMAM diblock copolymer thin films. Three well distinct film states are successfully prepared by the combination of amphiphilicity and the co-nonsolvency effect. The exposure of the thin films to a nitrogen flow, pure water vapor, and mixed water/acetone (90 vol%/10 vol%) vapor switches the films from a dried, to a hydrated (solvated, swollen), and to a water/acetone-exchanged (solvated, contracted) equilibrium state. These three states have distinctly different film thicknesses and solvent contents, which can be used as switch positions “off,” “on,” and “standby.”

Besides demonstrating the three different nanoswitch positions, the corresponding swelling and contraction kinetics are studied. A two-step behavior is identified for the film swelling (slow swelling phase, followed by a rapid swelling phase), whereas the film contraction occurs as a single, rapid process. The accelerated responsive behavior during the late swelling

phase, as well as the rapid film contraction process, is attributed to the cooperative hydration character of the PNIPMAM hydration shell, due to the hydrophobic moieties located on the polymer backbone and the side chain of the NIPMAM motif. To achieve fast response times of PNIPMAM-based materials, this implies that a minimum hydration level, or more generally solvation level, is needed for operating within the swelling regime dominated by cooperative hydration. Otherwise, at low levels of hydration, the polymer–polymer hydrophobic interactions are dominant.

On the molecular scale, the hydration shell around the PNIPMAM amide and isopropyl functional groups is built up and depleted as is expected for hydration and co-nonsolvency-induced film contraction, as hydrogen bonds are formed with the N–H and C=O groups, and water is structured around the isopropyl group. The process is partially reversed as acetone is added.

In conclusion, the found swelling characteristics imply, that PNIPMAM-based thin films can be used in ternary nanoswitches. They may be especially suitable for switching scenarios, in which a nanoswitch changes from a partially hydrated to a fully hydrated or from a fully hydrated to a water-/cosolvent-exchanged state. In these scenarios, the nanoswitch response would profit from the observed accelerating effect of cooperative hydration around the hydrophobic groups during the film swelling and contraction, respectively.

## 5. Experimental Section

*Materials for the Synthesis of PMMA-*b*-PNIPMAM:* Benzene (≥99.5%, Carl Roth), acetone (≥99%, Merck), diethyl ether (≥99.8%, Th. Geyer), pentane (≥99%, Roth), ethyl acetate (99.9%, VWR Chemicals), *N*-methyl-2-pyrrolidone (NMP, 99.5%, Alfa Aesar), lithium bromide (≥99%, Acros), and deuterated dichloromethane (DCM, 99.5 atom%, abcr) were used as received. Water (H<sub>2</sub>O) was deionized to a resistivity of 18.2 MΩ × cm using a Milli-Q Plus purification system (Merck Millipore, Darmstadt, Germany). Methyl methacrylate (≥99.0%, stabilized with >10 ppm hydroquinone monomethyl ether, Merck) was distilled immediately before use. *N*-isopropylmethacrylamide (NIPMAM, 97%, Aldrich) was crystallized four times from petroleum ether (boiling range 40–60 °C, VWR Chemicals, distilled before use). 2,2'-Azobis(isobutyronitrile) (AIBN, >98%, Fluka) was crystallized from methanol (technical grade, VWR Chemicals, distilled before use). The synthesis of the fluorophore-labeled chain transfer agent 2-(6-(dimethylamino)-1,3-dioxo-1H-benzo[de]isoquinolin-2(3H)-yl)ethyl-4-cyano-4-((phenethylthio) carbonothioyl) thio) pentanoate (CTA) is described in another study.<sup>[65]</sup>

*Synthesis of PMMA-*b*-PNIPMAM:* The block copolymer (PMMA-*b*-PNIPMAM) was synthesized by reversible addition fragmentation chain transfer (RAFT) polymerization in two consecutive steps, following an analogous procedure described in the study by Ko et al.<sup>[66]</sup> A detailed description of the synthesis procedure can be found in the Supporting Information. Assuming an ideal RAFT mechanism<sup>[67]</sup> as well as a negligible amount of initiator-derived polymer chains, the theoretically expected number average molar mass  $M_n^{\text{theo}}$  can be approximated by

$$M_n^{\text{theo}} = \frac{\text{conversion} \times M_{\text{monomer}} \times [M]}{[\text{CTA}]} + M_{\text{CTA}} \quad (1)$$

where  $M_{\text{monomer}}$  is the molar mass of the monomer,  $[M]$  is the initial molar concentration of the monomer,  $[\text{CTA}]$  is the molar concentration of chain transfer agent, and  $M_{\text{CTA}}$  is the molar mass of the chain transfer agent.

*UV–vis:* UV–vis absorption spectra were recorded on a UV/vis/NIR Spectrometer Lambda instrument (PerkinElmer). Quartz cuvettes with an optical path length of 10 mm were used. From the UV–vis spectra

of the polymers in ethyl acetate, number-average molar masses ( $M_n^{\text{vis}}$ ) were calculated by end-group analysis via Equation (2), assuming that every macromolecule carries exactly one naphthalimide chromophore moiety.

$$M_n^{\text{vis}} = \frac{\epsilon \cdot m_o \cdot d}{A \cdot V} \quad (2)$$

where  $\epsilon$  is the extinction coefficient,  $A$  the absorbance of the sample at  $\lambda_{\text{max}} = 409$  nm,  $c$  the molar concentration of the polymer,  $d$  the optical path length of the cuvette,  $M_n^{\text{vis}}$  the number average molar mass,  $m_o$  the mass of the polymer, and  $V$  the volume of solvent.

The chromophore's extinction coefficient in the polymers was assumed to be the same as in the low-molar-mass CTA (R)-2-(6-(dimethylamino)-1,3-dioxo-1H-benzo[de]isoquinolin-2(3H)-yl)ethyl 4-cyano-4-(phenethylthio)carbonothioylthio)pentanoate ( $\epsilon = 9800$  ( $\pm 3\%$ )  $\text{L mol}^{-1} \text{cm}^{-1}$ ) at maximum absorbance wavelength  $\lambda_{\text{max}} = 409$  nm in ethyl acetate).<sup>[66]</sup>

<sup>1</sup>H NMR: <sup>1</sup>H NMR spectra were recorded with a Bruker Avance 300 spectrometer (300 MHz) at ambient temperature in deuterated chloroform ( $\text{CDCl}_3$ ). For the PMMA macro-CTA, the number average degree of polymerization ( $DP_n$ ) and the corresponding number average molar mass ( $M_n^{\text{NMR}}_{\text{PMMA}}$ ) were determined from the <sup>1</sup>H NMR spectra by end-group analysis, comparing the integrals of a signal characteristic for the PMMA constitutional repeating unit ( $-\text{O}-\text{CH}_3$  at 3.6 ppm) with a signal group characteristic for the R-group of the CTA (naphthyl C2, C5, and C7 at 8.4–8.7). For the PNIPMAM block in the PMMA-*b*-PNIPMAM copolymer,  $DP_n$  was determined by comparing the integrals of signals characteristic for the two blocks ( $-\text{O}-\text{CH}_3$  at 3.6 ppm for PMMA and  $-\text{CON}-\text{CH}<$  at 4.0 ppm for PNIPMAM), assuming that  $DP_n$  of the PMMA block in the copolymer was identical to the one of the macro-CTA used. These  $DP_n$  values were used to calculate the number average molar masses ( $M_n^{\text{NMR}}_{\text{copolymer}}$ ) of the block copolymer.

**Size-Exclusion Chromatography (SEC):** SEC of the polymers was conducted at 25 °C in NMP + 0.5% LiBr as the eluent, with a set up consisting of an TSP P1000 isocratic pump (Thermo Fisher Scientific, Dreieich, Germany), a Shimadzu RID-6A refractive index detector (Shimadzu Corporation, Kyoto, Japan.), and a PSS GRAM column (7  $\mu\text{m}$ , 8  $\times$  300 mm) (PSS GmbH, Mainz, Germany). The SEC setup was calibrated using narrowly distributed poly(methyl methacrylate) standards.

**Elemental Analysis:** Quantitative determinations of percentages of nitrogen, carbon, hydrogen, and sulfur were conducted using a FlashEA 1112 CHNS/O Automatic Elemental Analyzer with MAa2O6R autosampler (Thermo Scientific).

**Materials for Thin-film Preparation:** Silicon wafers (p/Bor, <100>,  $d = 525 \pm 25$   $\mu\text{m}$ , 10–20  $\Omega \times \text{cm}$ ) were purchased from Si-Mat, Kaufering, Germany, and used as substrates (precut area: 20  $\times$  20  $\text{mm}^2$  for in-lab SR, 70  $\times$  70  $\text{mm}^2$  for simultaneous ToF-NR/SR, 10  $\times$  10  $\text{mm}^2$  for FTIR spectroscopy). For the substrate cleaning procedure, sulfuric acid ( $\text{H}_2\text{SO}_4$ , 95–98%, Aldrich) and hydrogen peroxide ( $\text{H}_2\text{O}_2$ , 30% aq., Roth) were used as received. Water was deionized to a resistivity of 18.2  $\text{M}\Omega \times \text{cm}$  using a Milli-Q Plus purification system (Merck Millipore, Burlington, U.S.A.). For preparation of the polymer solutions, 1,4-dioxane ( $\geq 99.5\%$ , Aldrich) was used as received. A solution of PMMA-*b*-PNIPMAM in 1,4-dioxane ( $c = 20$   $\text{mg mL}^{-1}$ ) was prepared, homogenized on a lab shaker for 24 h, and filtered (PTFE, pore size 0.2  $\mu\text{m}$ ).

**Materials for Vapor Generation:** Deuterated water ( $\text{D}_2\text{O}$ , 99.95%, Deutero), acetone ( $\text{CH}_3\text{COCH}_3$ ,  $\geq 99.8\%$ , Roth), and acetone- $d_6$  ( $\text{CD}_3\text{COCOD}_3$ , 99.80%, Deutero) were used as received. Water ( $\text{H}_2\text{O} > 99.98\%$ ) was deionized to a resistivity of 18.2  $\text{M}\Omega \times \text{cm}$  using a Milli-Q Plus purification system (Merck Millipore, Burlington, U.S.A.).

**Sample Preparation for ToF-NR/SR:** Pre-cut silicon wafers were cleaned in an acid bath (54 mL deionized water, 84 mL  $\text{H}_2\text{O}_2$ , 198 mL  $\text{H}_2\text{SO}_4$ ) at 75 °C (15 min), thoroughly rinsed with deionized water, and dried using compressed  $\text{N}_2$ . Thin films were deposited from solution via spin coating (2500 rpm, 60 s).

**Sample Preparation for FTIR Spectroscopy:** Precut silicon wafers were cleaned with oxygen plasma (0.4 mbar, 250 W, 10 min). Polymer films were prepared via drop casting the polymer solution (droplet volume

$V = 8.0$   $\mu\text{L}$ , positioned in the substrate center with a pipette) and subsequent drying 1 h before further handling.

**Thermal Annealing:** Immediately after their preparation, all samples were annealed (rate = 60 °C  $\text{h}^{-1}$ ,  $T_{\text{max}} = 150^\circ$ , 6 h) within a muffle furnace (Nabertherm, Lilienthal, Germany) to remove any residual 1,4-dioxane from the spin-coating/drop-casting process.

**Solvent Vapor Stimuli:** A custom-made vapor generation system provided a gas flow with tunable composition, for which dry  $\text{N}_2$ , saturated water vapor, and saturated acetone vapor streams were combined. A feeding tube led the gas flow to the respective sample environments allowing in situ ToF-NR/SR or FTIR measurements. A flow set point of 100% was equivalent with a constant gas flow rate of 1  $\text{L min}^{-1}$ . The vapor generation system, feeding tube, and sample environments were integrated into a single thermostat cycle (JULABO FP50 HL, JULABO Labortechnik GmbH, Seelbach, Germany). The temperature  $T_{\text{set}} = 18^\circ\text{C}$  was kept constant for all experiments.

**ToF-NR and SR:** All ToF-NR/SR measurements were carried out using a specialized sample environment featuring aluminum windows and liquid channels inside the walls and lid to ensure a homogeneous temperature.<sup>[68]</sup> ToF-NR measurements were carried out at the horizontal neutron reflectometer REFSANS at the Heinz Maier-Leibnitz Zentrum (MLZ) in Garching, Germany.<sup>[69]</sup> Specular reflectivity data were analyzed using the Motofit plugin<sup>[70]</sup> for IGOR PRO v7.08 (WaveMetrics, Portland, U.S.A.), to yield the thin-film SLD profiles along the surface normal  $z$ . Specifications about the ToF-NR instrument configuration, measurement modes, data reduction, and data analysis are presented in the Supporting Information. SR measurements were carried out with a Filmetrics F20 thin-film analyzer and evaluated using the FILMeasure software (KLA, Milpitas, U.S.A.). White light ( $\lambda = 380$ –1100 nm) was focused (spot  $\varnothing = 2.0$  mm) onto the sample using an optical fiber and lens assembly mounted above a  $\text{CaF}_2$  window in the lid of the sample environment. The reflected spectra were recorded and fitted in 10 s intervals, which allowed monitoring the film thickness  $d$  and refractive index  $n(\lambda)$  in situ.

**FTIR Spectroscopy:** FTIR spectra were collected using an Equinox 55 FTIR spectrometer (Bruker Optik GmbH, Rosenheim, Germany). Specifications about the instrument configuration and measurement parameters are presented in the Supporting Information. For all measurements, samples were mounted inside a custom-made sample environment with ZnS windows. FTIR spectra were recorded within the wavenumber range of  $\nu = 600$ –4000  $\text{cm}^{-1}$ . To determine the absorbance peak area of the O–D stretching vibration signal, integration limits were set to  $\nu_{\text{min}} = 2300$   $\text{cm}^{-1}$  and  $\nu_{\text{max}} = 2745$   $\text{cm}^{-1}$ . Shifts within the peak positions of selected signals were obtained by fitting Gaussian functions.

## Supporting Information

Supporting Information is available from the Wiley Online Library or from the author.

## Acknowledgements

The authors thank Deutsche Forschungsgemeinschaft (DFG) for financial support (LA 611/16-1, MU 1487/29-1, PA 771/20-1). L.P.K. and T.W. acknowledge funding through the German Ministry for Education and Research (BMBF) project “FlexiProb” (grant no. 05 K2016). P.W. acknowledges the China Scholarship Council (CSC). The Heinz Maier-Leibnitz Zentrum and the neutron reflectometer REFSANS are acknowledged for beam time allocation and providing excellent equipment and support of measurements. The authors thank S. Schiffer for providing acetone- $d_6$ . The authors gratefully acknowledge SEC support by S. Prenzel and H. Schlaad (Universität Potsdam).

Open access funding enabled and organized by Projekt DEAL.

## Conflict of Interest

The authors declare no conflict of interest.

## Data Availability Statement

The data that support the findings of this study are available from the corresponding author upon reasonable request.

## Keywords

co-nonsolvency, diblock copolymers, nanoswitches, neutron reflectometry, thin films

Received: February 12, 2021

Revised: March 29, 2021

Published online:

- [1] A. S. Hoffman, *Macromol. Symp.* **1995**, *98*, 645.
- [2] M. A. C. Stuart, W. T. S. Huck, J. Genzer, M. Müller, C. Ober, M. Stamm, G. B. Sukhorukov, I. Szleifer, V. V. Tsukruk, M. Urban, F. Winnik, S. Zauscher, I. Luzinov, S. Minko, *Nat. Mater.* **2010**, *9*, 101.
- [3] M. Wei, Y. Gao, X. Li, M. J. Serpe, *Polym. Chem.* **2017**, *8*, 127.
- [4] M. Hruby, P. Štěpánek, J. Pánek, C. M. Papadakis, *Colloid Polym. Sci.* **2019**, *297*, 1383.
- [5] M. Heskins, J. E. Guillet, *J. Macromol. Sci. Part A* **1968**, *2*, 1441.
- [6] S. Fujishige, K. Kubota, I. Ando, *J. Phys. Chem.* **1989**, *93*, 3311.
- [7] V. Aseyev, H. Tenhu, F. M. Winnik, *Adv. Polym. Sci.* **2011**, *242*, 29.
- [8] A. Halperin, M. Kröger, F. M. Winnik, *Angew. Chem., Int. Ed.* **2015**, *54*, 15342.
- [9] K. Otake, R. Karaki, T. Ebina, C. Yokoyama, S. Takahashi, *Macromolecules* **1993**, *26*, 2194.
- [10] H. G. Schild, D. A. Tirrell, *J. Phys. Chem.* **1990**, *94*, 4352.
- [11] F. M. Winnik, H. Ringsdorf, J. Venzmer, *Macromolecules* **1990**, *23*, 2415.
- [12] S. Kunugi, Y. Yamazaki, K. Takano, N. Tanaka, M. Akashi, *Langmuir* **1999**, *15*, 4056.
- [13] M. Shibayama, K. Isono, S. Okabe, T. Karino, M. Nagao, *Macromolecules* **2004**, *37*, 2909.
- [14] Y. Zhang, S. Furry, D. E. Bergbreiter, P. S. Cremer, *J. Am. Chem. Soc.* **2005**, *127*, 14505.
- [15] B. Ebeling, S. Eggers, M. Hendrich, A. Nitschke, P. Vana, *Macromolecules* **2014**, *47*, 1462.
- [16] D. Mukherji, C. M. Marques, K. Kremer, *Annu. Rev. Condens. Matter Phys.* **2020**, *11*, 271.
- [17] Y. Kotsuchibashi, M. Ebara, T. Aoyagi, R. Narain, *Polymers* **2016**, *8*, 380.
- [18] C. M. Papadakis, P. Müller-Buschbaum, A. Laschewsky, *Langmuir* **2019**, *35*, 9660.
- [19] Q. Yu, J. Cho, P. Shivapooja, L. K. Ista, G. P. Lopez, *ACS Appl. Mater. Interfaces* **2013**, *5*, 9295.
- [20] C. Alvarez-Lorenzo, A. Concheiro, *Chem. Commun.* **2014**, *50*, 7743.
- [21] Y. Yu, M. Cirelli, B. D. Kieviet, E. S. Kooij, G. J. Vansco, S. de Beer, *Polymer* **2016**, *102*, 372.
- [22] Y. Yu, R. A. Lopez de la Cruz, B. D. Kieviet, H. Gojzweski, A. Pons, G. J. Vansco, S. de Beer, *Nanoscale* **2017**, *9*, 1670.
- [23] M. Kanidi, A. Papagiannopoulos, A. Skandalis, M. Kandyła, S. Pispas, *J. Polym. Sci., Part B: Polym. Phys.* **2019**, *57*, 670.
- [24] S. Ashraf, H.-K. Park, H. Park, S.-H. Lee, *Macromol. Res.* **2016**, *24*, 297.
- [25] J.-P. Couturier, M. Sütterlin, A. Laschewsky, C. Hettrich, E. Wischerhoff, *Angew. Chem., Int. Ed.* **2015**, *54*, 6641.
- [26] H. R. Culver, J. R. Clegg, N. A. Peppas, *Acc. Chem. Res.* **2017**, *50*, 170.
- [27] L. Hu, Q. Zhang, X. Li, M. J. Serpe, *Mater. Horiz.* **2019**, *6*, 1774.
- [28] E. Wischerhoff, N. Badi, J.-F. Lutz, A. Laschewsky *Soft Matter* **2010**, *6*, 705.
- [29] S. Schmidt, M. Zeiser, T. Hellweg, C. Duschl, A. Fery, H. Möhwald, *Adv. Funct. Mater.* **2010**, *20*, 3235.
- [30] H. Kim, H. Witt, T. A. Oswald, M. Tarantola, *ACS Appl. Mater. Interfaces* **2020**, *12*, 33516.
- [31] W. Wang, G. Kaune, J. Perlich, C. M. Papadakis, A. M. Bivigou Koumba, A. Laschewsky, K. Schlage, R. Röhlberger, S. V. Roth, R. Cubitt, P. Müller-Buschbaum, *Macromolecules* **2010**, *43*, 2444.
- [32] P. Shi, C. M. Amb, A. L. Dyer, J. R. Reynolds, *ACS Appl. Mater. Interfaces* **2012**, *4*, 6512.
- [33] P. Xu, L. Murtaza, J. Shi, M. Zhu, Y. He, H. Yu, O. Goto, H. Meng, *Polym. Chem.* **2016**, *7*, 5351.
- [34] A. Buchberger, S. Peterka, A. M. Coclite, A. Bergmann, *Sensors* **2019**, *19*, 999.
- [35] W. Wang, E. Metwalli, J. Perlich, C. M. Papadakis, R. Cubitt, P. Müller-Buschbaum, *Macromolecules* **2009**, *42*, 9041.
- [36] W. Wang, E. Metwalli, J. Perlich, K. Troll, C. M. Papadakis, R. Cubitt, P. Müller-Buschbaum, *Macromol. Rapid Commun.* **2009**, *30*, 114.
- [37] L. P. Kreuzer, C. Lindenmeir, C. Geiger, T. Widmann, V. Hildebrand, A. Laschewsky, C. M. Papadakis, P. Müller-Buschbaum, *Macromolecules* **2021**, *54*, 1548.
- [38] E. I. Tiktopulo, V. N. Uversky, V. B. Lushchik, S. I. Klenin, V. E. Bychkova, O. B. Ptitsyn, *Macromolecules* **1995**, *28*, 7519.
- [39] J. Spěváček, J. Dybal, *Macromol. Symp.* **2014**, *336*, 39.
- [40] H. Kouřilová, L. Hanyková, J. Spěváček, *Eur. Polym. J.* **2009**, *45*, 2935.
- [41] V. Chytrý, M. Netopiřík, M. Bohdanecký, K. Ulbrich, *Macromol. Rapid Commun.* **1997**, *18*, 107.
- [42] Y. Maeda, T. Nakamura, I. Ikeda, *Macromolecules* **2001**, *34*, 8246.
- [43] Y. C. Tang, Y. W. Ding, G. Z. Zhang, *J. Phys. Chem. B* **2008**, *112*, 8447.
- [44] J. Dybal, M. Trchova, P. Schmidt, *Vib. Spectrosc.* **2009**, *51*, 44.
- [45] C.-H. Ko, K.-L. Claude, B.-J. Niebuur, F. A. Jung, J.-J. Kang, D. Schanzenbach, H. Frielinghaus, L. C. Barnsley, B. Wu, V. Pipich, A. Schulte, P. Müller-Buschbaum, A. Laschewsky, C. M. Papadakis, *Macromolecules* **2020**, *53*, 6816.
- [46] S. Nieuwenhuis, Q. Zhong, E. Metwalli, L. Bießmann, M. Philipp, A. Miasnikova, A. Laschewsky, C. M. Papadakis, R. Cubitt, J. Wang, P. Müller-Buschbaum, *Langmuir* **2019**, *35*, 7691.
- [47] J. Pang, H. Yang, J. Ma, R. S. Cheng, *J. Theor. Comput. Chem.* **2011**, *10*, 359.
- [48] S. A. Deshmukh, S. K. R. S. Sankaranarayanan, K. Suthar, D. C. Mancini, *J. Phys. Chem. B* **2012**, *116*, 2651.
- [49] R. O. R. Costa, R. F. S. Freitas, *Polymer* **2002**, *43*, 5879.
- [50] G. Zhang, C. Wu, *J. Am. Chem. Soc.* **2001**, *123*, 1376.
- [51] F. Tanaka, T. Koga, H. Kojima, N. Xue, F. M. Winnik, *Macromolecules* **2011**, *44*, 2978.
- [52] D. Mukherji, C. M. Marques, K. Kremer, *Nat. Commun.* **2014**, *5*, 4882.
- [53] I. Bischofberger, D. C. E. Calzolari, V. Trappe, *Soft Matter* **2014**, *10*, 8288.
- [54] P.-W. Zhu, L. Chen, *Phys. Rev. E* **2019**, *99*, 22501.
- [55] E. Krieg, W. E. Shih, *Angew. Chem., Int. Ed.* **2018**, *57*, 714.
- [56] K. Volk, J. P. S. Fitzgerald, P. Ruckdeschl, M. Retsch, T. A. F. König, M. Karg, *Adv. Opt. Mater.* **2017**, *5*, 1600971.
- [57] Y. Zhang, W. S. P. Carvalho, C. Farg, M. J. Serpe, *Sens. Actuators, B* **2019**, *290*, 520.
- [58] S. Nian, L. Pu, *J. Org. Chem.* **2019**, *84*, 909.
- [59] X. Wang, H. Huang, H. Liu, F. Rehfeldt, X. Wang, K. Zhang, *Macromol. Chem. Phys.* **2019**, *220*, 1800562.
- [60] L. P. Kreuzer, T. Widmann, N. Hohn, K. Wang, L. Bießmann, L. Peis, J.-F. Moulin, V. Hildebrand, A. Laschewsky, C. M. Papadakis, P. Müller-Buschbaum, *Macromolecules* **2019**, *52*, 3486.

- [61] T. Widmann, L. P. Kreuzer, N. Hohn, L. Bießmann, K. Wang, S. Rinner, J.-F. Moulin, A. J. Schmid, Y. Hannapel, O. Wrede, M. Kühnhammer, T. Hellweg, R. von Klitzing, P. Müller-Buschbaum, *Langmuir* **2019**, *35*, 16341.
- [62] L. P. Kreuzer, T. Widmann, L. Bießmann, N. Hohn, J. Pantle, R. Märkl, J.-F. Moulin, V. Hildebrand, A. Laschewsky, C. M. Papadakis, P. Müller-Buschbaum, *Macromolecules* **2020**, *53*, 2841.
- [63] Y. Okada, F. Tanaka, *Macromolecules* **2005**, *38*, 4465.
- [64] H. Kojima, *Polym. J.* **2018**, *50*, 411.
- [65] V. Hildebrand, A. Laschewsky, D. Zehm, *J. Biomater. Sci., Polym. Ed.* **2014**, *25*, 1602.
- [66] C.-H. Ko, C. Henschel, G. P. Meledam, M. A. Schroer, P. Müller-Buschbaum, A. Laschewsky, C. M. Papadakis, *Macromolecules* **2021**, *54*, 384.
- [67] C. Barner-Kowollik, M. Buback, B. Charleux, M. L. Coote, M. Drache, T. Fukuda, A. Goto, B. Klumperman, A. B. Lowe, J. B. McLeary, G. Moad, M. J. Monteiro, R. D. Sanderson, M. P. Tonge, P. Vana, *J. Polym. Sci. A Polym. Chem.* **2006**, *44*, 5809.
- [68] T. Widmann, L. P. Kreuzer, G. Mangiapia, M. Haese, H. Frielinghaus, P. Müller-Buschbaum, *Rev. Sci. Instrum.* **2020**, *91*, 113903.
- [69] J.-F. Moulin, M. Haese, *J. Large-Scale Res. Facil.* **2015**, *1*, 9.
- [70] A. Nelson, *J. Appl. Crystallogr.* **2006**, *39*, 273.